Research Article | Vol. 9, No. 7 | 1 Jul 2018 | BIOMEDICAL OPTICS EXPRESS 2905
Biomedical Optics EXPRESS

# Quantitative diagnosis of tissue microstructure with wide-field high spatial frequency domain imaging

WEIHAO LIN,[1] BIXIN ZENG,[1] ZILI CAO,[1] XINLIN CHEN,[1] KAIYAN YANG,[2] AND MIN XU[1,3,*]

[1]*Institute of Lasers and Biophotonics, Department of Biomedical Engineering, Wenzhou Medical University, Wenzhou 325035, China*
[2]*Department of Pathology and Laboratory Medicine, The First Affiliated Hospital of Wenzhou Medical University, Wenzhou 325035, China*
[3]*Department of Physics, Fairfield University, Fairfield, CT 06824, USA*
**mxu@fairfield.edu*

**Abstract:** Non-contact and minimally invasive endoscopic optical imaging is an invaluable diagnostic tool for tissue examination and cancer screening. The point sampling techniques with high sensitivity to the tissue microenvironment are time consuming and often not affordable in clinics. There is a major clinical need for a large field-of-view (FOV) rapid screening method to highlight subtle tissue microstructural alterations. To address this unmet need, we have developed High Spatial Frequency Domain Imaging (HSFDI)–a non-contact imaging modality that spatially maps the tissue microscopic scattering structures over a large field of view (>1cm$^2$). Based on an analytical reflectance model of sub-diffusive light from forward-peaked highly scattering media, HSFDI quantifies the spatially-resolved parameters of the light scattering phase function (i.e., the backscattering probability and the light spreading length) from the reflectance of structured light modulated at high spatial frequencies. Enhanced signal to noise ratio (SNR) is achieved at even ultra-high modulation frequencies with single snapshot multiple frequency demodulation (SSMD). The variations in tissue microstructures, including the strength of the background (pudding) refractive index fluctuation and the prominent scattering structure (plum) morphology, can then be inferred. After validation with optical phantoms, measurements of fresh *ex vivo* tissue samples revealed significant contrast and differentiation of the phase function parameters between different types and disease states (normal, inflammatory, and cancerous) of tissue whereas tissue absorption and reduced scattering coefficients only show modest changes. HSFDI may provide wide-field images of microscopic structural biomarkers unobtainable with either diffuse light imaging or point-based optical sampling. Potential clinical applications include the rapid screening of excised tissue and the noninvasive examination of suspicious lesions during operation.



**OCIS codes:** (170.3660) Light propagation in tissues; (170.3880) Medical and biological imaging; (170.6935) Tissue characterization.

## References and links

1. B. Chance, "Optical method," Annu. Rev. Biophys. Biophys. Chem. **20**(1), 1–30 (1991).
2. A. Yodh, B. Tromberg, E. Sevick Muraca, and D. Pine, eds.,"Diffusing photons in turbid media," J. Opt. Soc. Am. A **14**, 136–342 (1997).
3. B. C. Wilson, "Detection and treatment of dysplasia in Barrett's esophagus: a pivotal challenge in translating biophotonics from bench to bedside," J. Biomed. Opt. **12**(5), 051401–051422 (2007).
4. M. R. Austwick, B. Clark, C. A. Mosse, K. Johnson, D. W. Chicken, S. K. Somasundaram, K. W. Calabro, Y. Zhu, M. Falzon, G. Kocjan, T. Fearn, S. G. Bown, I. J. Bigio, and M. R. Keshtgar, "Scanning elastic scattering spectroscopy detects metastatic breast cancer in sentinel lymph nodes," J. Biomed. Opt. **15**(4), 047001 (2010).
5. I. Itzkan, L. Qiu, H. Fang, M. M. Zaman, E. Vitkin, I. C. Ghiran, S. Salahuddin, M. Modell, C. Andersson, L. M. Kimerer, P. B. Cipolloni, K. H. Lim, S. D. Freedman, I. Bigio, B. P. Sachs, E. B. Hanlon, and L. T. Perelman,

#326261 https://doi.org/10.1364/BOE.9.002905
Journal © 2018 Received 19 Mar 2018; revised 9 May 2018; accepted 20 May 2018; published 4 Jun 2018

Biomedical Optics EXPRESS

"Confocal light absorption and scattering spectroscopic microscopy monitors organelles in live cells with no exogenous labels," Proc. Natl. Acad. Sci. U.S.A. **104**(44), 17255–17260 (2007).
6. V. Backman and H. K. Roy, "Light-scattering technologies for field carcinogenesis detection: a modality for endoscopic prescreening," Gastroenterology **140**(1), 35–41 (2011).
7. L. Cherkezyan, I. Capoglu, H. Subramanian, J. D. Rogers, D. Damania, A. Taflove, and V. Backman, "Interferometric spectroscopy of scattered light can quantify the statistics of subdiffractional refractive-index fluctuations," Phys. Rev. Lett. **111**(3), 033903 (2013).
8. S. D. Konecky, A. Mazhar, D. Cuccia, A. J. Durkin, J. C. Schotland, and B. J. Tromberg, "Quantitative optical tomography of sub-surface heterogeneities using spatially modulated structured light," Opt. Express **17**(17), 14780–14790 (2009).
9. J. Vervandier and S. Gioux, "Single snapshot imaging of optical properties," Biomed. Opt. Express **4**(12), 2938–2944 (2013).
10. T. D. O'Sullivan, A. E. Cerussi, D. J. Cuccia, and B. J. Tromberg, "Diffuse optical imaging using spatially and temporally modulated light," J. Biomed. Opt. **17**(7), 071311 (2012).
11. S. C. Kanick, D. M. McClatchy, V. Krishnaswamy, J. T. Elliott, K. D. Paulsen, and B. W. Pogue, "Sub-diffusive scattering parameter maps recovered using wide-field high-frequency structured light imaging," Biomed. Opt. Express **5**(10), 3376–3390 (2014).
12. A. J. Lin, M. A. Koike, K. N. Green, J. G. Kim, A. Mazhar, T. B. Rice, F. M. LaFerla, and B. J. Tromberg, "Spatial frequency domain imaging of intrinsic optical property contrast in a mouse model of Alzheimer's disease," Ann. Biomed. Eng. **39**(4), 1349–1357 (2011).
13. A. M. Laughney, V. Krishnaswamy, E. J. Rizzo, M. C. Schwab, R. J. Barth, D. J. Cuccia, B. J. Tromberg, K. D. Paulsen, B. W. Pogue, and W. A. Wells, "Spectral discrimination of breast pathologies *in situ* using spatial frequency domain imaging," Breast Cancer Res. **15**(4), R61 (2013).
14. X. Chen, W. Lin, C. Wang, S. Chen, J. Sheng, B. Zeng, and M. Xu, "*In vivo* real-time imaging of cutaneous hemoglobin concentration, oxygen saturation, scattering properties, melanin content, and epidermal thickness with visible spatially modulated light," Biomed. Opt. Express **8**(12), 5468–5482 (2017).
15. J. R. Mourant, J. Boyer, A. H. Hielscher, and I. J. Bigio, "Influence of the scattering phase function on light transport measurements in turbid media performed with small source-detector separations," Opt. Lett. **21**(7), 546–548 (1996).
16. F. Bevilacqua and C. Depeursinge, "Monte Carlo study of diffuse reflectance at source–detector separations close to one transport mean free path," JOSA A **16**(12), 2935–2945 (1999).
17. K. W. Calabro and I. J. Bigio, "Influence of the phase function in generalized diffuse reflectance models: review of current formalisms and novel observations," J. Biomed. Opt. **19**(7), 075005 (2014).
18. M. A. Neil, R. Juškaitis, and T. Wilson, "Method of obtaining optical sectioning by using structured light in a conventional microscope," Opt. Lett. **22**(24), 1905–1907 (1997).
19. V. Krishnaswamy, J. T. Elliott, D. M. McClatchy, R. J. Barth, W. A. Wells, B. W. Pogue, and K. D. Paulsen, "Structured light scatteroscopy," J. Biomed. Opt. **19**(7), 070504 (2014).
20. D. M. McClatchy, E. J. Rizzo, W. A. Wells, P. P. Cheney, J. C. Hwang, K. D. Paulsen, B. W. Pogue, and S. C. Kanick, "Wide-field quantitative imaging of tissue microstructure using sub-diffuse spatial frequency domain imaging," Optica **3**(6), 613–621 (2016).
21. J. M. Schmitt and G. Kumar, "Optical scattering properties of soft tissue: a discrete particle model," Appl. Opt. **37**(13), 2788–2797 (1998).
22. M. Xu, T. T. Wu, and J. Y. Qu, "Unified Mie and fractal scattering by cells and experimental study on application in optical characterization of cellular and subcellular structures," J. Biomed. Opt. **13**(2), 024015 (2008).
23. M. Xu and R. R. Alfano, "Fractal mechanisms of light scattering in biological tissue and cells," Opt. Lett. **30**(22), 3051–3053 (2005).
24. M. Xu, "Diagnosis of the phase function of random media from light reflectance," Sci. Rep. **6**(1), 22535 (2016).
25. M. Xu, Z. Cao, W. Lin, X. Chen, L. Zheng, and B. Zeng, "Single snapshot multiple frequency modulated imaging of subsurface optical properties of turbid media with structured light," AIP Adv. **6**(12), 125208 (2016).
26. M. Xu, "Plum pudding random medium model of biological tissue toward remote microscopy from spectroscopic light scattering," Biomed. Opt. Express **8**(6), 2879–2895 (2017).
27. W. Lin, Z. Cao, B. Zeng, and M. Xu, "Quantitative modulated imaging of turbid media in the high spatial frequency domain," Proc. SPIE **9701**, 97010Y (2016).
28. A. N. Bashkatov, E. A. Genina, and V. V. Tuchin, "Optical properties of skin, subcutaneous, and muscle tissues: a review," J. Innov. Opt. Health Sci. **4**(1), 9–38 (2011).

## 1. Introduction

One central tenet in the application of light in biology and medicine is noninvasive diagnosis of the structure and function of tissue from tissue-light interaction [1]. Non-contact and minimally invasive endoscopic optical imaging is an invaluable diagnostic tool for tissue examination and cancer screening. As tissue microstructure represents the refractive index variation which scatters light, scattered light by tissue has been used extensively to identify

Biomedical Optics EXPRESS

structural alterations or heterogeneities in tissue due to disease or physiological variations [2,3]. Fiber-optics based [4] and confocal [5] techniques have been successfully used to detect such changes in the superficial layer of tissue. The subwavelength features of microstructures at tens of nanometers have been quantified with scattered light as well with point spectroscopic detection [6,7]. A critical drawback of those approaches for clinical applications is that cumbersome and time consuming raster scanning is required for wide-field imaging and often not affordable in clinics.

Wide-field tissue imaging over field of view of $1cm^2$ or larger is, however, usually not capable of resolving tissue microstructure. For example, diffuse optical imaging (DOI) by multiple scattering light is limited to the mapping of the reduced scattering coefficient on the overall scattering densities. Nevertheless, diffuse optical imaging is unique in being able to quantify both absorption and scattering properties of tissue simultaneously. Consequently one form of DOI, Spatial Frequency Domain Imaging (SFDI) has attracted significant attention recently as one non-contact and quantitative wide field modality for rapid mapping of the optical properties of turbid media such as biological tissue from reflectance measurement [8–14]. The sensitivity to ultrastructural changes is gained by sub-diffusive light at a close source-detector separation or a high spatial modulation [15–17]. By measuring tissue reflectance modulated at a moderate high spatial frequency ($<1mm^{-1}$), such SFDI can recover one additional scattering parameter (the $\gamma$ parameter)–an implicit metric of the size-scale distribution of scattering features [18–20]. There are, however, still some notable limitations with the above method. The morphological details and the microscopic structure of the random medium are encoded in the phase function of the medium which describes the angular distribution of the scattered light upon single interaction with the medium [21–23]. The phase function represents the ultimate information about the microenvironment of the medium that can be retrieved remotely. One would desire to quantify the whole phase function rather than one partial measure such as the $\gamma$ parameter. Furthermore, higher spatial modulation frequencies are preferable as their sensitivity to the microstructure is enhanced. These limitations arise mainly from two factors: first the lack of an analytical model relating the reflectance of sub-diffusive light to the explicit form of the phase function, and second the degradation of the signal to noise ratio for the modulated reflectance preventing higher spatial frequencies to be applied. Lifting these limitations and enabling modulated light to robustly image the phase function may open up a novel platform of genuinely imaging tissue microstructure over a large field of view with structured light. The significant and even dramatic contrast and differentiation between different types and disease states (normal, inflammatory, and cancerous) of tissue revealed below illustrates such platform to be potentially invaluable for the diagnosis of biological and other random media.

In this paper, we present High Spatial Frequency Domain Imaging (HSFDI)–a non-contact imaging modality that for the first time spatially diagnoses the phase function and maps the tissue microscopic scattering structures over a large field of view ($>1cm^2$). Based on an analytical reflectance model of sub-diffusive light from forward-peaked highly scattering media [24], HSFDI quantifies the map of the backscattering probability $p_\pi$ and the light spreading length $l_\Theta$ governing sub-diffusive light from the reflectance of structured light modulated at high spatial frequencies ($>1mm^{-1}$). The deterioration in the signal to noise ratio (SNR) at higher modulation frequencies in SFDI is overcome with Single Snapshot Multiple frequency Demodulation (SSMD) [25]. Enhanced SNR is achieved at even ultra-high modulation frequencies in HSFDI. The variations in tissue microstructures including the strength of the background (pudding) refractive index fluctuation and the prominent scattering structure (plum) morphology can then be inferred [26]. After validation with optical phantoms, measurements of fresh *ex vivo* tissue samples revealed significant contrast and differentiation of the microstructural parameters between different types and disease states of tissue whereas tissue absorption and reduced scattering coefficients only show modest change. Our results suggest HSFDI may provide wide-field images of microscopic

Biomedical Optics EXPRESS

structural biomarkers unobtainable with either diffuse light imaging or point-based optical sampling. HSFDI suits well various clinical applications including rapid screening of excised tissue and noninvasive examination of suspicious lesions during operation.

## 2. Methods

### *2.1 Reflectance of sub-diffusive light from forward-peaked scattering media*

Light scattering in turbid media such as biological tissue is a complex process as light propagation is governed by the radiative transport (RT) and the most commonly used diffusion approximation to RT breaks down at a short source-detector separation [16]. It is well recognized that reflectance of sub-diffusive light which has suffered few scattering events and remits nearby the incident point is highly sensitive to the phase function (and microstructure) of the scattering medium. An analytical formulism for sub-diffusive reflectance on the exact form of phase function has only been derived recently which established a theoretical foundation for HSFDI [24, 27]. The analytical model incorporates the small-angle scattering approximation (SAA) to radiative transport for sub-diffusive light reflectance at a close source-detector separation and expresses the dependence of the light reflectance from forward-peaked scattering media on the phase function of the scattering medium in a closed form.

Briefly the backscattered light in the forward-peaked scattering medium constitutes three kinds of contributions: SAA photons which have experienced multiple small angle scattering and exactly one large angle scattering, snake photons which experience exactly two large angle scattering, and diffusive photons which experience more than two large angle scattering. The reflectance profile at an arbitrary separation and over the full spatial frequency has been provided [24]. The reflectance of sub-diffusive light is dominated by SAA photons and takes a simple form:

$$I_{SAA}(\mathrm{q}) = \frac{1}{2} p_\pi \left[ 1 + 2 \cdot 6^{1/3} \Gamma(\frac{4}{3}) (1_\Theta \mathrm{q})^{-2/3} \right] \tag{1}$$

for a spatially modulated plane wave at frequency $q>>\mu_s'$ and of unit power where $p_\pi$ is the backscattering probability and $l_\Theta \equiv \Theta/\mu_s$ is the spreading length scale governing the angular spreading of sub-diffusive photons. Here the reduced scattering coefficient $\mu_s'$ equals to $\mu_s(1\text{-}g)$, $\mu_s$ is the scattering coefficient, and $g$ is the mean cosine of scattering angles. The arbitrary phase function $p(\theta)$ of the scattering medium is mapped to:

$$p_{SAA}(\theta) = \frac{1-2p_b}{\pi\Theta^2} \exp(-\frac{\theta^2}{\Theta^2}) + \frac{1}{2\pi} p_b \tag{2}$$

In Eq. (2), the parameter $p_b \approx 2\pi p(\pi) = 2\pi p_\pi$ is the percentage of light which is backscattered into the back hemisphere. The mean squared root scattering angle $\Theta$ is associated with the prominent scattering structures in tissue and decreases with their size. The former reflects the strength of the refractive index fluctuation (pudding) and the latter the morphology of the prominent scattering centers (plum) in tissue, respectively [24,26]. Reflectance measurement at multiple high spatial frequencies hence can be used to determine $p_\pi$ and $l_\Theta$ via Eq. (1) and to infer the microstructure of the medium.

### *2.2 High spatial frequency domain imaging*

Spatial frequency domain imaging (SFDI) is a wide-field and non-contact method that uses spatially modulated structured illumination patterns: $I_{IN} = I_{DC}^{(0)} + I_{AC}^{(0)} \cos(2\pi f_x x + \alpha)$, the reflectance takes the form:

$$I_{OUT} = I_{DC} + I_{AC}(x) \cos(2\pi f_x x + \alpha) \tag{3}$$

Biomedical Optics EXPRESS

where the ratio $I_{AC}(x)$ over $I_{AC}^{(0)}$ represents Modulation Transfer Function (MTF) of reflectance which in turbid media is determined by its optical properties. Three-phase demodulation from three measurements taken at α, α + 2π/3, and α + 4π/3 phase delays are commonly used to extract $I_{AC}(x)$. This demodulation requires three images and, more importantly, suffers from deteriorating SNR and fails at higher spatial modulation frequencies. HSFDI uses an alternative Single Snapshot Multiple frequency Demodulation technique (SSMD) [25]. SSMD makes use of the orthogonality of harmonic functions to extract multiple modulation components simultaneously from a single structured-illuminated image at once. SSMD exhibits excellent noise suppression in imaging, particularly suitable for high modulation frequency imaging [25].

To gain the sensitivity to the phase function (and microstructure) of turbid media, HSFDI operates at high spatial modulation frequencies (>1mm$^{-1}$). Unlike conventional SFDI setup applicable for low spatial frequency imaging, HSFDI requires both high fidelity and high spatial resolution for modulated illumination and optical imaging systems. The HSFDI instrument is shown schematically in Fig. 1. For the sake of aberration optimization, centered optical configuration is designed using pellicle beam splitter to integrate the modulated illumination system and imaging system without introducing ghosting. The light source is Digital Micromirror Device (DMD, DLP LightCrafter 4500, Texas Instruments) and the red channel (623nm) was used in the reported experiments. The DMD was operated in the pattern mode and the trigger time for one displayed image was set at 10ms. A Canon 5D Mark III camera was used to record the reflectance images with its exposure time set at 50ms. As the output light intensity from the DMD is not linear, calibration was performed to correct this nonlinearity by comparing to the diffuse reflectance from a Lambertian reflectance standard. The modulation transfer function (MTF) of the optical system was also calibrated by imaging resolution test targets (R1L1S1P, Thorlabs, Inc.) over the spatial frequency range. The diffuse reflectance from the Lambertian reflectance standard was used to obtain the illumination intensity, with which the absolute MTF of specimens is determined. The illuminated area on the surface of the specimen was 13mm × 13mm field of view in the reported experiments. The resolution of HSFDI system in the object space is 7.7μm × 7.7μm. The maximum modulated spatial frequency that could be achieved with minimal distortion is 3.33 mm$^{-1}$ limited by the DMD. The data acquisition speed of HSFDI is very rapid as only a single frame of image is required for reflectance measurement at each high spatial frequency, and it takes approximately 0.3s to accomplish six high spatial frequencies measurements.

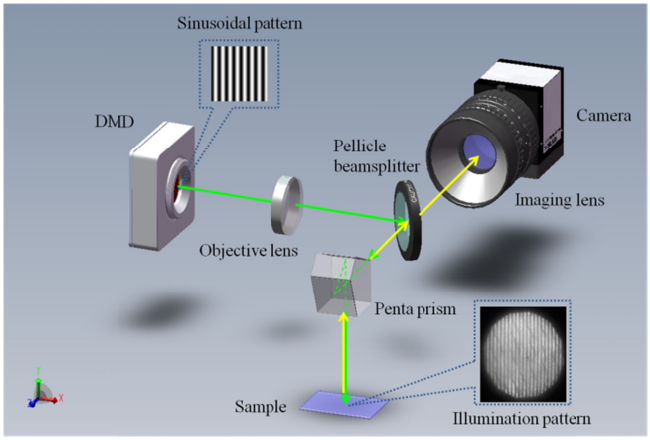


Fig. 1. Schematic diagram of the DMD-based HSFDI system. The structured beam is magnified and projected onto the specimen. Backscattered light from the specimen is imaged onto the camera after passing through the imaging objective.

Biomedical Optics EXPRESS

## 3. Results and discussion

### *3.1 Validation with polystyrene sphere suspensions*

To test HSFDI in the recovery of phase function parameters ($p_\pi$ and $l_\Theta$), we prepared suspensions of mixed polystyrene spheres. 1.25ml polystyrene sphere suspension of diameter 1.5μm (5.0% concentration) was first diluted by 6.75ml distilled water to yield a measured $\mu_s' = 1.25\text{mm}^{-1}$ at the probing wavelength λ = 623nm. The measured $\mu_s'$ is lower than the theoretical value ($2.03\text{mm}^{-1}$) owing to the precipitation of 1.5μm polystyrene spheres. Then polystyrene sphere suspension of diameter 0.1μm (2.5% concentration) was added at 0.5ml intervals. Such a mixed suspension emulates light scattering by biological tissue with the larger spheres representing the plum and the smaller spheres the pudding following the Plum and Pudding Random Media model for biological tissue [26]. Each mixed suspension was imaged by HSFDI at spatial frequencies of $f_x$ = [1/0.9, 1/0.75, 1/0.6, 1/0.45, 1/0.3] $\text{mm}^{-1}$ to recover the phase function parameters $p_\pi$ and $l_\Theta$. The reduced scattering coefficient $\mu_s'$ was also obtained from measurement at a lower spatial frequency $f_x$ = 1/3.6 $\text{mm}^{-1}$.

Traditional SFDI suffers from the deterioration in SNR at higher modulation frequencies. Single Snapshot Multiple frequency Demodulation (SSMD) [25] is used in HSFDI which significantly improves the SNR and allows the high-fidelity imaging at a spatial frequency much higher than $1\text{mm}^{-1}$. Figure 2 exhibits the recovered MTF and their standard deviations of light reflectance of one typical mixed suspension (mixing with 0.50ml diameter 0.1μm polystyrene spheres) by the standard three-phase demodulation method and SSMD method. SSMD shows much smaller standard deviations than the standard three-phase method and, in particular, SSMD performs well at higher frequencies whereas the standard three-phase demodulation fails (MTF should decrease with the modulation frequency).

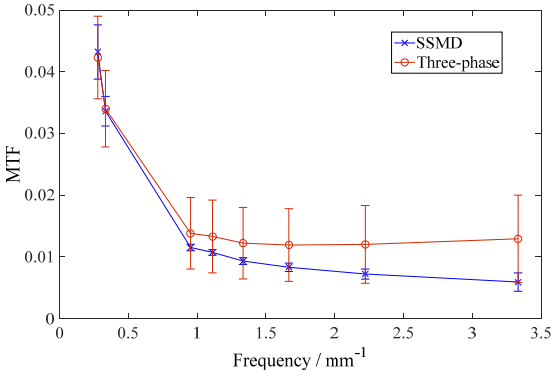


Fig. 2. The MTF and standard deviation of light reflectance of one typical mixed suspension with 0.50ml diameter 0.1μm polystyrene spheres retrieved by the standard three-phase method and SSMD method.

The sub-diffusive light reflectance Eq. (1) agrees well with the experimental measurement (see Fig. 3). The retrieved $\mu_s'$ and phase function parameters $p_\pi$ and $l_\Theta$ for various mixed polystyrene sphere suspensions are displayed in Fig. 4. The theoretical curves are computed from the weighted average of large and small polystyrene spheres. In particular, the backscattering probability $p_\pi$ of 0.1μm polystyrene sphere and 1.5μm polystyrene sphere is 1/4π and 0.0011, respectively. The theoretical value of $p_\pi$ for the mixed suspension is given by:

$$P_{\pi\_mixed} = \frac{p_{\pi 1}\cdot\mu_{s1} + p_{\pi 2}\cdot\mu_{s2}}{\mu_{s1}+\mu_{s2}} \tag{4}$$

Biomedical Optics EXPRESS

where subscripts 1 and 2 represent 1.5μm polystyrene sphere and 0.1μm polystyrene sphere, respectively. We observe overall excellent agreement between the experimentally retrieved parameters and the theoretical values. Both $p_\pi$ and $\mu_s'$ increases progressively as more suspension of polystyrene sphere of diameter 0.1μm was added. Furthermore, $l_\Theta$ remains steady overall until the added volume of 0.1μm polystyrene sphere suspension reached 2.0ml, jumping from 0.030mm to 0.042mm. This indicates that the large amount of 0.1μm polystyrene sphere has elevated the isotropic scattering background above a threshold that the mean squared root scattering angle $\Theta$ no longer depends on the large scatterer alone.

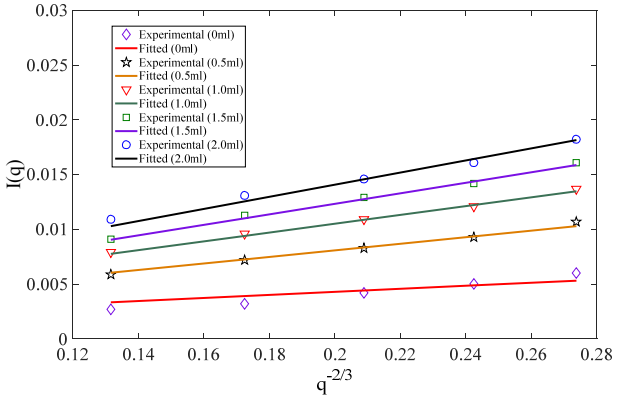


Fig. 3. Sub-diffusive light reflectance Eq. (1) provides an excellent fitting to the measured light reflectance for various mixed polystyrene sphere suspensions of diameter 1.5μm and 0.1μm.

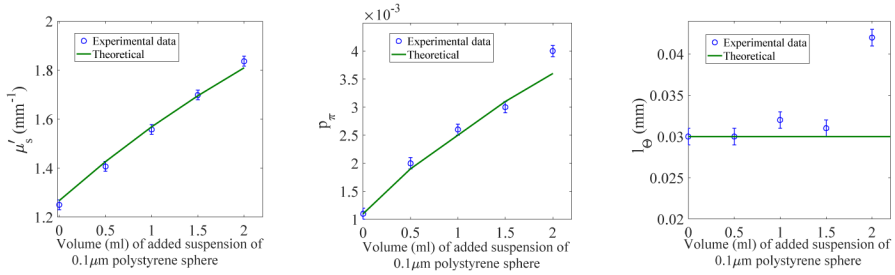


Fig. 4. Comparison between extracted and theoretical $\mu_s'$ and phase function parameters for various mixed polystyrene sphere suspensions of diameter 1.5μm and 0.1μm.

### 3.2 Tissue type discrimination

The advantage of HSFDI technique to discriminate tissue microstructure was then demonstrated by imaging porcine and chicken tissue specimens over an area of size 10mm × 10mm at high modulation frequencies [1/0.9, 1/0.75, 1/0.6, 1/0.45, and 1/0.3] $mm^{-1}$. The absorption coefficient $\mu_a$ and the reduced scattering coefficient $\mu_s'$ were also imaged from measurement at a lower spatial frequency $f_x = 1/3.6$ $mm^{-1}$. The phase function contrast is from the ultrastructural differences in muscle, adipose, skin and tendon tissue. Table 1 summarizes $\mu_a$, $\mu_s'$ and phase function parameters $p_\pi$, $l_\Theta$ for porcine (muscle, adipose, skin, and tendon) and chicken (muscle and skin) specimens. The extracted absorption and reduced scattering coefficients ($\mu_a$, $\mu_s'$) of porcine muscle and skin agree with the values reported in the literature [28]. The phase function parameters $p_\pi$ and $l_\Theta$ exhibit much improved structural contrast comparing to the reduced scattering coefficient $\mu_s'$. Different tissue types are all well separated except between porcine and chicken skins (see Fig. 5).

Biomedical Optics EXPRESS

**Table 1. The absorption and reduced scattering coefficients $\mu_a$, $\mu_s'$ and phase function parameters $p_\pi$, $l_\Theta$ for various porcine and chicken tissue types. The standard deviation is computed for the values over the imaged region.**

| Tissue type | $\mu_a$ (mm$^{-1}$) | $\mu_s'$ (mm$^{-1}$) | $p_\pi$ | $l_\Theta$ (mm) |
|---|---|---|---|---|
| Porcine muscle | 0.1846 ± 0.0071 | 0.9187 ± 0.0354 | 0.0049 ± 0.0029 | 0.0131 ± 0.0102 |
| Porcine adipose | 0.0237 ± 0.0036 | 1.4528 ± 0.0863 | 0.0049 ± 0.0030 | 0.0076 ± 0.0052 |
| Porcine skin | 0.0697 ± 0.0046 | 0.9682 ± 0.0354 | 0.0091 ± 0.0006 | 0.1915 ± 0.0069 |
| Porcine tendon | 0.0224 ± 0.0019 | 0.6045 ± 0.0224 | 0.0175 ± 0.0016 | 0.1880 ± 0.0089 |
| Chicken muscle | 0.0143 ± 0.0011 | 0.3168 ± 0.0128 | 0.0003 ± 0.0001 | 0.0110 ± 0.0067 |
| Chicken skin | 0.0239 ± 0.0024 | 0.8980 ± 0.0333 | 0.0082 ± 0.0018 | 0.1660 ± 0.0107 |

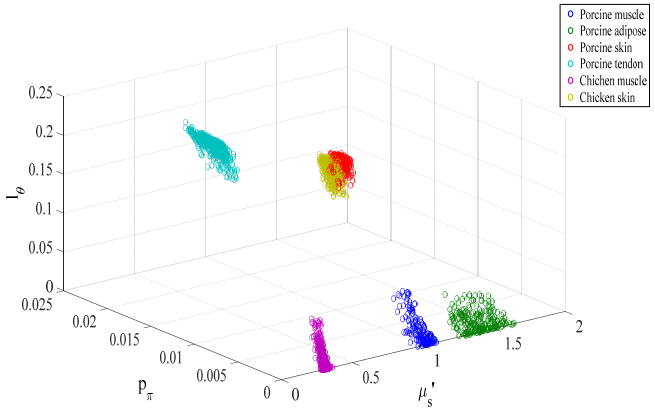


Fig. 5. The triple (the reduced scattering coefficient $\mu_s'$, and the phase function parameters $p_\pi$, $l_\Theta$) for various porcine and chicken tissue types is well separated except between porcine and chicken skins.

### 3.3 Ex vivo cervical carcinoma tissue imaging

HSFDI was then used to image surgically excised human cervix tissue and evaluated against co-registered histopathological analysis a pilot study. A fresh surgically excised human cervix tissue was cut to a size of approximately 6mm × 12mm × 3mm. After HSFDI imaging, the standard procedure was followed to prepare a frozen section of the top layer of the tissue sample through formaldehyde fixation and H&E staining. The surface section matched the HSFDI maps well in shape other than slight distortions caused by histological processing.

White light photograph of the cervical tissue specimen and the retrieved maps of $\mu_s'$, $p_\pi$ and $l_\Theta$ are displayed in Fig. 6(a-d) together with the H&E stained histological images for four highlighted representative regions including normal cervical tissue, slight inflammation, severe inflammation, and invasive squamous-cell carcinoma in Fig. 6(e-h). Please note that a trained pathologist provided detailed pathological evaluations of tissue section based on morphological features such as cell differentiation, nuclear to cytoplasmic ratio, and production of extra-cellular collagen. Besides the four regions shown in Fig. 6, we have also analyzed other randomly selected regions on the sample, comparing their optical parameters and the pathological evaluations. The absorption and reduced scattering coefficients $\mu_a$, $\mu_s'$, phase function parameters $p_\pi$, $l_\Theta$, and the morphology indicator $\Theta(1\text{-}g)$ for these regions of different disease states are summarized in Table 2.

Biomedical Optics EXPRESS

**Table 2. The absorption and reduced scattering coefficients $\mu_a$, $\mu_s'$, phase function parameters $p_\pi$, $l_\Theta$, and the morphology indicator $\Theta(1\text{-}g) = l_\Theta \cdot \mu_s'$ for different disease states of the human cervix tissue. The standard deviation is computed for the values over the highlighted region.**

| | $\mu_a$ (mm$^{-1}$) | $\mu_s'$ (mm$^{-1}$) | $p_\pi$ | $l_\Theta$ (mm) | $\Theta(1\text{-}g)$ |
|---|---|---|---|---|---|
| Normal cervical tissue | 0.0176 ± 0.0013 | 0.8995 ± 0.0617 | 0.0034 ± 0.0015 | 0.0183 ± 0.0081 | 0.0163 ± 0.0077 |
| Slight inflammation | 0.0253 ± 0.0026 | 1.1541 ± 0.1378 | 0.0056 ± 0.0047 | 0.0227 ± 0.0140 | 0.0297 ± 0.0188 |
| Severe inflammation | 0.0474 ± 0.0075 | 1.2563 ± 0.0880 | 0.0186 ± 0.0063 | 0.0382 ± 0.0158 | 0.0432 ± 0.0162 |
| Invasive carcinoma | 0.0401 ± 0.0036 | 1.4121 ± 0.2447 | 0.0457 ± 0.0133 | 0.1007 ± 0.0407 | 0.1608 ± 0.0825 |

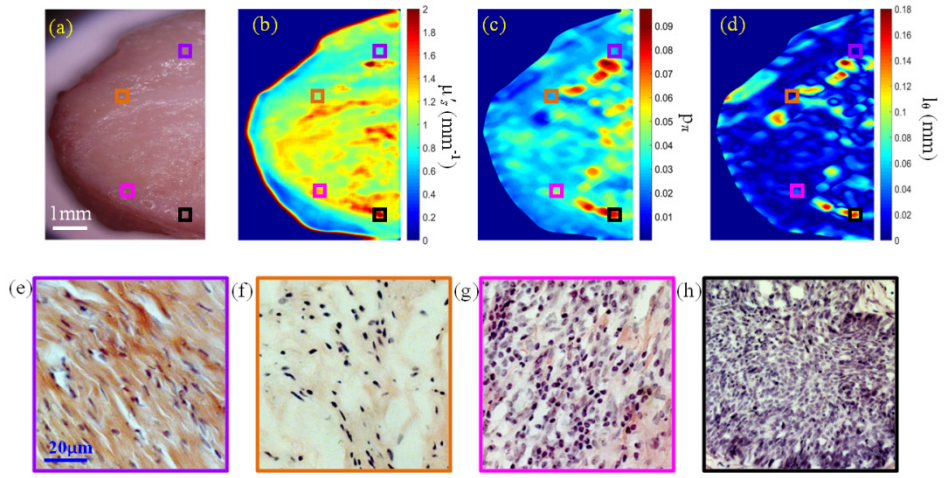


Fig. 6. (a) Photograph of cervical carcinoma tissue specimen; (b) The retrieved $\mu_s'$ map; (c) The retrieved $p_\pi$ map; (d) The retrieved $l_\Theta$ map; (e-h) H&E stained histological images for the four highlighted regions in (a-d) including normal cervical tissue (violet), slight inflammation (orange), severe inflammation (pink), and invasive squamous-cell carcinoma (black).

Significant contrast is observed in $p_\pi$, $l_\Theta$ between the different disease states. The steady increase of $p_\pi$, $l_\Theta$ from normal cervical tissue, slight inflammation, severe inflammation, to invasive squamous-cell carcinoma quantifies the enhancement in the background refractive index fluctuation (pudding) and the shrinkage of the size of the prominent scattering centers (plum) [26]. The morphology indicator $\Theta(1\text{-}g)$ computed by the product of $\mu_s'$ and $l_\Theta$ captures the pure microstructural characteristics (and is independent on the densities of the scatterers), demonstrating a dramatic contrast and differentiation between normal, inflammatory, and cancerous tissue. Different disease states of human cervix tissue are all well separated with HSFDI imaging (see Figs. 7-8). As one illustration of the potential application of HSFDI, the entire specimen could be classified according to the value of $\Theta(1\text{-}g)$ into different disease states based on Table 2 (see Fig. 7). The normal, slightly inflammatory, severely inflammatory, and cancerous regions are identified by the increasing morphology indicator. To quantitatively assess disease state discrimination on cervix tissue, box and whisker plots have been given in Fig. 9 for each optical scatter parameter. The two-sample t-tests have also been performed between each pair of tissue types. The resulting p-values are tabulated in Fig. 10 for all three scatter parameters, $p_\pi$, $l_\Theta$, $\mu_s'$ and the morphology indicator $\Theta(1\text{-}g)$, with a blue color indicating a significant p-value at the $p < 0.05$ level. A smaller p-value suggests a more significant discrimination power between two different disease states of tissues. It is remarkable that the new phase function parameters ($p_\pi$, $l_\Theta$) and $\Theta(1\text{-}g)$ unlike the reduced

Biomedical Optics EXPRESS

scattering coefficient $\mu_s'$ can distinguish cancer, severely inflammatory and other disease states (see Fig. 10).

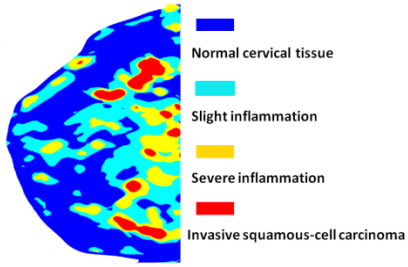


Fig. 7. Classification of different disease states (normal, slightly inflammatory, severely inflammatory, and cancerous) of cervical tissue specimen according to the value of the morphology indicator $\Theta(1\text{-}g)$ .

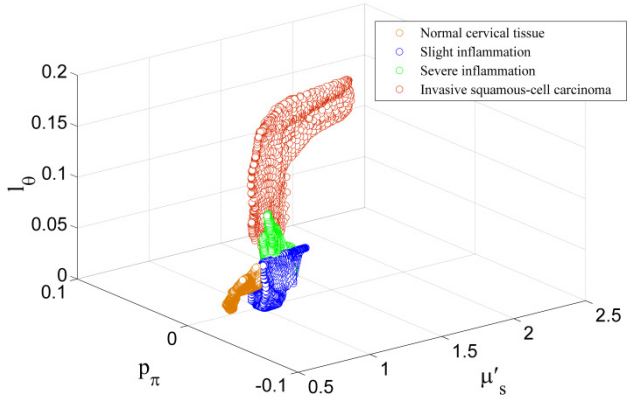


Fig. 8. The triple (the reduced scattering coefficient $\mu_s'$, and the phase function parameters $p_\pi$, $l_\Theta$) differentiates well the various disease states of human cervix tissue.

Biomedical Optics EXPRESS

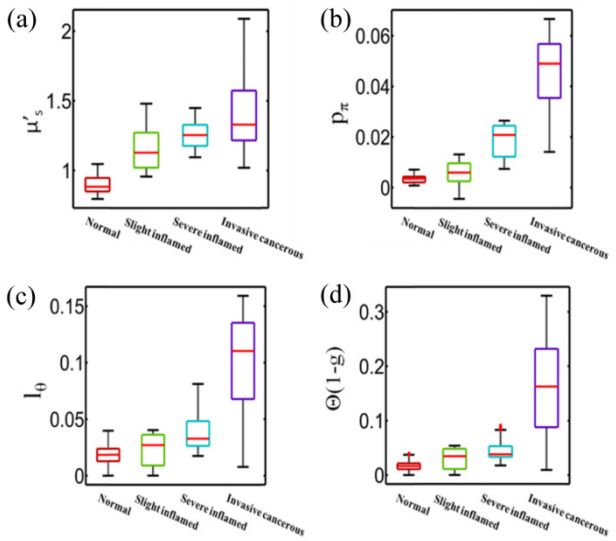


Fig. 9. Box and whisker plots for all points used in the cluster analysis for (a) $\mu_s'$, (b) $p_\pi$, (c) $l_\Theta$ and (d) $\Theta(1\text{-}g)$.

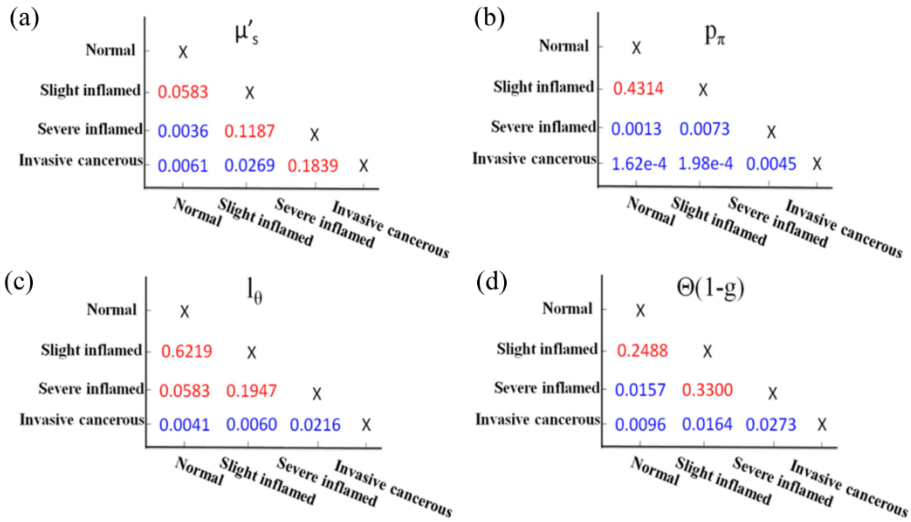


Fig. 10. The two-sample t-test p-values for each pairwise combination of tissue diagnoses with each scatter parameter (a) $\mu_s'$, (b) $p_\pi$,(c) $l_\Theta$ and (d) $\Theta(1\text{-}g)$. The blue color indicates a significant p-value at the $p < 0.05$ level. A smaller p-value suggests a more significant discrimination power between two different disease states of tissues.

These data demonstrate the ability of HSFDI to rapidly assess whole-tissue specimen where point-source or microscopic-based tissue interrogation methods would have to randomly sample a large number of locations to achieve similar robustness. Moreover, the phase function parameters $p_\pi$, $l_\Theta$ and the morphology indicator $\Theta(1\text{-}g)$ recovered by HSFDI is highly sensitive to microstructural alterations. The backscattering probability ($p_\pi$) reflects the strength of the background refractive index fluctuation (pudding), the spreading length ($l_\Theta$) is associated with the morphology of the prominent scattering centers (plum), and the morphology indicator captures the pure density-independent characteristics of the microstructure. These microstructural biomarkers exhibit significant contrast and

Biomedical Optics EXPRESS

differentiation between normal, inflammatory, and cancerous tissue. For example, the morphology indicator was observed to have a contrast of 4:1 or above between cancerous and noncancerous human cervix tissue (see Table 2). Such a contrast and differentiation is significantly stronger than those obtained in earlier efforts in sub-diffusive SFDI ($<1mm^{-1}$) [20] whose γ parameter varied between 1.5 and 1.8 for different breast tissue (fibroglandular, benign fibroadenoma, and invasive carcinoma). This can be attributed to the significantly enhanced sensitivity to the microstructure for HSFDI operating at much higher spatial modulation frequencies ($>1mm^{-1}$) through innovations in both theoretical modeling and demodulation techniques. Although the number of specimens studied here is limited, the promising results suggest HSFDI may provide wide-field images of microscopic structural biomarkers unobtainable with either diffuse light imaging or point-based optical sampling. We envision that HSFDI may be applied in various clinical applications including rapid screening of excised tissue and noninvasive examination of suspicious lesions during operation.

## 4. Conclusions

We have presented High Spatial Frequency Domain Imaging (HSFDI)–a non-contact imaging modality that spatially maps the tissue microscopic scattering structures over a large field of view ($>1cm^2$). HSFDI quantifies the spatially-resolved microstructural parameters of the medium from the reflectance of structured light modulated at high spatial frequencies. The variations in tissue microstructures including the strength of the background (pudding) refractive index fluctuation and the prominent scattering structure (plum) morphology are then inferred by the recovered light backscattering probability, the spreading length, and the morphology indicator. After validation with optical phantoms, measurements of fresh *ex vivo* tissue samples have revealed significant contrast and differentiation of the microstructural parameters between different types and disease states of tissue whereas tissue absorption and reduced scattering coefficients only show modest change. HSFDI may emerge as one promising rapid wide-field modality imaging tissue microstructure with potential clinical applications in rapid screening of excised tissue and noninvasive examination of suspicious lesions during operation.

## Funding

Natural Science Foundation of Zhejiang Province (LZ16H180002); National Natural Science Foundation of China (81470081); Wenzhou Municipal Science and Technology Bureau (ZS2017022); Wenzhou Municipal Science and Technology Bureau (Y20170219); National Science Foundation, USA (1607664).

## Acknowledgments

We thank Xue J for clinical support.

## Disclosures

We report a patent application related to the technology and analysis methods described in this study. The authors declare that there are no other conflicts of interest related to this article.